Dalton Transactions

ROYAL SOCIETY OF CHEMISTRY

PAPER

View Article Online
View Journal | View Issue

Cite this: *Dalton Trans.*, 2024, **53**, 16871

Gelatin and sodium alginate derived carbon/silicon composites as high-performance anode materials for lithium-ion batteries†

Liyang Lin,[a,b] Mengjun Li,[a,b] Ying Yan,[d] Yuanhao Tian,[d] Juan Qing[a] and Susu Chen*[c]

Received 14th September 2024,
Accepted 23rd September 2024

DOI: 10.1039/d4dt02623c

rsc.li/dalton

The volume expansion and poor conductivity greatly limit the application of silicon as an anode for lithium-ion batteries. Although nanocrystallization of silicon and its surface carbon coating can be improved to some extent, the serious problems of particle aggregation and structural instability have not been effectively solved. In this paper, gelatin and sodium alginate (GE + SA) derived carbon/silicon composites are successfully prepared by a liquid-phase method, the freeze-drying technique, and heat treatment. Si nanoparticles (NPs) are uniformly encapsulated in a three-dimensional network of N-doped carbon that is enriched with a rich pore structure. The reversible capacity of the particular Si@C composite electrode was maintained at 580 mA h g^{-1} after 300 cycles at a current density of 1 A g^{-1}, showing good cycling stability. Meanwhile, the anode also has excellent rate performance with reversible capacities of 2230, 1458, 1101, and 686.6 mA h g^{-1} at current densities of 0.1, 0.5, 1, and 2 A g^{-1}, respectively. The GE + SA derived carbon/silicon composites effectively solve the problems of particle aggregation and an unstable carbon/silicon interface structure and can become candidates for anode materials in lithium-ion batteries.

1. Introduction

In recent years, with the increasing demand for various high-power electronic products such as electric vehicles and unmanned aerial vehicles (UAVs), the performance of lithium-ion batteries (LIBs) does not meet the requirements. Therefore, key indicators such as the energy density of LIBs need to be further improved.[1–5] Graphite is currently the most widely used anode material for LIBs, but its low theoretical specific capacity (327 mA h g^{-1}) limits the further applications.[6–9] Silicon stands out with an extremely high theoretical specific capacity (4200 mA h g^{-1}) and a low operating potential, making it a promising anode material.[10–13] However, there are many problems when using silicon as an anode material for LIBs. Silicon particles will have significant volume expansion with the occurrence of delithiation and lithiation, which leads to particle fragmentation as well as active material detachment, resulting in poor cycling performance.[14–16] At the same time, the high impedance of silicon is also one of the obstacles limiting its further development, and the low conductivity leads to its inability to be applied on a large scale. In order to solve the above problems, researchers have proposed a variety of strategies, including nanostructure engineering, preparation of porous silicon, and silicon–carbon composite technology.[17–22]

As one of the most commonly used methods, silicon–carbon composite technology aims to enhance the stability and electrical conductivity of the composite material through the introduction of carbon coating. In addition, the introduction of carbon coating can effectively alleviate the volume expansion of silicon. Currently, the commonly used carbon sources include CNTs, CNFs, GO, MXenes, amorphous carbon, *etc*. Although the variety of carbon sources is very large, most of them, without exception, suffer from the disadvantages of complicated preparation, unsustainability, and high cost, which directly hinder the processing of Si@C composites toward a commercial scale.[23–30] Therefore, in order to further promote the commercialization of Si@C composites, low-cost and abundant biomass carbon sources have received extensive attention. Biomass derived carbon has the advantages of low cost, richness and structural diversity, and it is rich in natural porous structures, which can not only effectively alleviate the

[a]*School of Aeronautics, Chongqing Jiaotong University, Chongqing 400074, China*
[b]*Chongqing Key Laboratory of Green Aviation Energy and Power, Chongqing Jiaotong University, Chongqing 400074, China*
[c]*Chongqing College of Mobile Communication, Chongqing 401520, China. E-mail: susuchen@cqu.edu.cn*
[d]*Southwest Technology and Engineering Research Institute, Chongqing 400039, China*

† Electronic supplementary information (ESI) available. See DOI: https://doi.org/10.1039/d4dt02623c

problem of volume expansion of silicon materials, but also further improve the overall electrical conductivity of the material, as well as practicing the development goal of green energy sources.[31] In addition, some of the biomass derived carbon materials are rich sources of natural nitrogen, which can further enhance the electrochemical properties of the materials. Therefore, biomass-based carbon and silicon composite modified materials have very great potential and prospects. For example, Sui *et al.* used lignin as a biomass carbon source and SiO_2 nanotubes (SNTs) as a silicon source to obtain SNTs@C-PDLF silicon–carbon composites by the colloidal method.[32] The electrochemical performance of the SNTs@C-PDLF anode was outstanding, which still had a capacity of 549 mA h g^{-1} after 800 cycles at a current density of 1 A g^{-1} and a good rate performance (a specific capacity of 262 mA h g^{-1} when the current density was increased to 3 A g^{-1}). Li *et al.* used lychee shells as a raw material of biomass and a high-energy ball milling and activator process to embed silicon nanoparticles into biomass derived carbon materials.[33] The 3D LAC@Si anode material exhibited excellent electrochemical performance, with a coulombic efficiency of up to 98.34% and a residual capacity of up to 834.4 mA h g^{-1} after cycling for 100 cycles at a current density of 0.2 A g^{-1}. In 2016, Zhang *et al.* prepared silicon/nitrogen-doped carbon/carbon nanotube (SNCC) nano/micro-structured spheres for the first time by electrospraying using rice husk-derived silicon as the silicon source and polyacrylonitrile (PAN) as the nitrogen source. The SNCC spheres exhibited good cycling performance, maintaining a specific capacity of 1031 mA h g^{-1} after 100 cycles at a current density of 0.5 A g^{-1}.[34] In 2019, Zhang *et al.* introduced SiO_x with a nitrogen-doped carbon coating using an MXene as a substrate. The as-prepared MXene/Si@SiO_x@C anodes exhibited excellent electrochemical performance after 1000 cycles at 10 C (1 C = 4200 mA g^{-1}), a coulombic efficiency of 99.9%, and a capacity retention of 76.4% with a reversible capacity of 390 mA h g^{-1}.[35] Biomass-derived N-doped carbon coatings have been widely applied to anode materials for lithium-ion batteries. However, the nitrogen sources commonly used in these studies suffer from a number of problems, including insufficient greening, high cost, and inconvenient use. To solve the above problems, we proposed to use the green and inexpensive gelatin and sodium alginate as the nitrogen and carbon sources. The surface of gelatin and sodium alginate (GE + SA) is rich in a large number of amino ($-NH_2$) and carboxyl (–COOH) groups, which makes it very soluble in water and shows good film-forming properties. The good water solubility and film-forming property can promote the homogeneous mixing of Si NPs with gelatin/sodium alginate (GE + SA) solution and can uniformly encapsulate Si NPs to form a uniform nitrogen-doped carbon coating.

In this study, the composite of biomass gelatin and sodium alginate is used as the carbon source, and the N-doped Si@C composite is obtained through *in situ* carbonization by utilizing the natural viscosity as well as the nitrogen element of gelatin. The results show that the N-doped carbon coating can effectively inhibit the phenomenon of volume expansion of Si NPs and significantly increase the Li^+ and electron transport rate, which improves both the overall stability of the composite material and its electrochemical properties. The effects of different components of the composites on the electrochemical properties are also investigated by combining various characterization techniques. The GE + SA derived carbon/silicon composite provides a feasible way for the industrialization of silicon-based anode materials.

2. Experimental

2.1 Materials

Gelatin (99%, biotech grade) and sodium alginate (AR, 90%) were obtained from Macklin, and Si NPs (99% metals basis, 60–100 nm) were provided by Aladdin. All chemical samples were used directly without further processing.

2.2 Preparation of Si@C

Si@C composites were prepared by colloidal coating and high temperature carbonization. First, gelatin was added to deionized water and stirred at 50 °C until complete dissolution, followed by the addition of sodium alginate, while the temperature of the water bath was changed to 75 °C, and stirring was continued until the dissolved state to obtain a solution with high viscosity. After that, Si NPs were added to the solution, and ultrasonic dispersion treatment was used for 0.5 h to make the Si NPs uniformly distributed in the solution, and a mixture with uniform color was obtained. Subsequently, it was stirred at room temperature for 2 h. Then it was frozen in an ultra-low temperature refrigerator for 24 h, followed by drying in a freeze dryer for 24 h to obtain the precursor. Finally, it was calcined in a tube furnace at 800 °C under an Ar atmosphere for 2 h to obtain the final product Si@C. Gelatin, sodium alginate, and GE + SA were used as the carbon sources, and the prepared Si@C composites were referred to as Si@C-G, Si@C-S, and Si@C-GS, respectively.

2.3 Characterization

X-ray diffraction (XRD, Rigaku Ultima IV) was used to analyze the crystal structure of the materials, a scanning electron microscope (SEM, Thermo Scientific Apreo 2C) and energy spectrometer (EDS, OXFORD ULTIM Max65) were used to observe the micro-morphology of the materials, and the internal morphology of the materials was examined by transmission electron microscopy (TEM). The degree of graphitization and the elements contained in the materials were analyzed by Raman spectroscopy (Thermo Scientific DXR2xi), and the chemically bound states were characterized by X-ray photoelectron spectroscopy (XPS, Thermo Fisher K-Alpha, with Al Kα as the X-ray source). The pore state and pore specific surface area were tested using a fully automated specific surface and porosity analyzer (BET, Micromeritics ASAP 2020).

2.4 Cell fabrication and electrochemical analysis

The performance of all the samples was tested using coin-type cells (CR2032). The active materials, acetylene black, and sodium alginate were mixed in deionized water in the ratio of 6 : 2 : 2 and coated on a high-purity copper foil, which was dried in a vacuum drying oven at 80 °C for 12 h to obtain the pole piece. The final electrode was cut into circular discs of 14 mm diameter with an areal coating density of 0.8 mg cm^{-2}. The pole piece was cut into small disks, and the cells were assembled in an Ar filled glove box (Mikrouna Co., Ltd China, O_2 and H_2O <0.01 ppm) with Li foil (Honjo Chemical Corp, 99.95%) as the counter electrode and a polypropylene membrane (Celgard 2500) was used as the diaphragm and a solution of 1.0 M $LiPF_6$ in ethylene carbonate, diethyl carbonate and dimethyl carbonate (1 : 1 : 1 vol%) was used as the electrolyte. Cyclic voltammetry (CV) tests were performed on an electrochemical workstation ((CorrTest, CS2350H)) with a voltage window of 0.01–1.5 V (*vs.* Li/Li^+) and a scan rate of 0.1–0.5 mV s^{-1}. Electrochemical impedance spectroscopy (EIS) was performed on an electrochemical workstation (CorrTest, CS2350H) with a frequency range of 0.01–10^5 Hz and an amplitude of 5 mV. The constant current test was performed with a voltage window of 0.01–1.5 V (*vs.* Li/Li^+) through the battery test system (Neware, Ct-4008Tn-5V50mA-HWX).

3. Results and discussion

Fig. 1 shows the specific preparation process of Si@C composites, and the main raw materials include gelatin, sodium alginate, and Si NPs. Firstly, gelatin and sodium alginate were dissolved by stirring at a suitable temperature, and then Si NPs were added for ultrasonic dispersion to obtain a colloid with uniform color. Gelatin and sodium alginate are rich in groups, which will be uniformly wrapped on the surface of Si NPs by electrostatic action, thus forming a three-dimensional linkage structure. A mixture with homogeneous texture is obtained by freeze-drying at low temperature. Finally, the Si@C-GS composites were obtained by calcination under an Ar atmosphere.

SEM images of Si NPs and Si@C-GS composites are shown in Fig. 2(a) and (b). The SEM image of commercial Si NPs is shown in Fig. 2(a). It can be seen that Si NPs with a size of about 100 nm are densely distributed. The SEM image of commercial Si NPs is shown in Fig. 2(b). Compared to the Si NPs, obvious carbon cladding layers can be seen in Si@C-GS, which suggests that gelatin and sodium alginate can form a homogeneous coating on the Si NPs, resulting in a three-dimensional carbon network structure.

In order to further explore the internal structure of Si@C-GS composites, we performed TEM and HRTEM tests, as shown in Fig. 2(c–f). In Fig. 2(c and d), obvious carbon coating layers can be seen, which are mainly composed of amorphous carbon, while Si NPs are uniformly embedded in them to form a stable silicon–carbon core–shell structure. Fig. 2(e and f) show the HRTEM images; the obvious carbon coating layer with a thickness of about 3–4 nm can be seen. According to Fig. 2(f), the width of the diffraction fringes is measured to be 0.31 nm, which can be indexed to the (111) diffraction plane of Si. In order to further compare the homogeneity of Si@C-G, Si@C-S and Si@C-GS composites carbon coatings, we performed TEM and HRTEM tests, as shown in Fig. S1(a–f).† In Fig. S1(a–c),† we can see that the Si NPs are loaded on the amorphous carbon network to form an obvious core–shell structure. Fig. S1(d–f)† show the HRTEM images of Si@C-G, Si@C-S and Si@C-GS composites, respectively, from which we can see more clearly that the Si particles are coated by interconnected amorphous carbon shells, forming a stable SiC composite structure. The thickness of the carbon cladding layer of Si@C-G varies from 1.94 nm at the thinnest point to 4.36 nm at the thickest point, while the cladding layer of Si@C-S is the thickest among the three samples and varies in thickness, with the thickest point of the cladding being 5.85 nm. Compared with the other two samples, the Si@C-GS composites show a more homogeneous cladding layer, with the Si NPs uniformly embedded in an amorphous carbon network and with a moderate thickness. The thickness of the coating is moderate, about 3.85 nm, and the uniform and appropriate thickness of the carbon coating can protect the Si NPs without limiting the release of the capacity of the Si NPs,

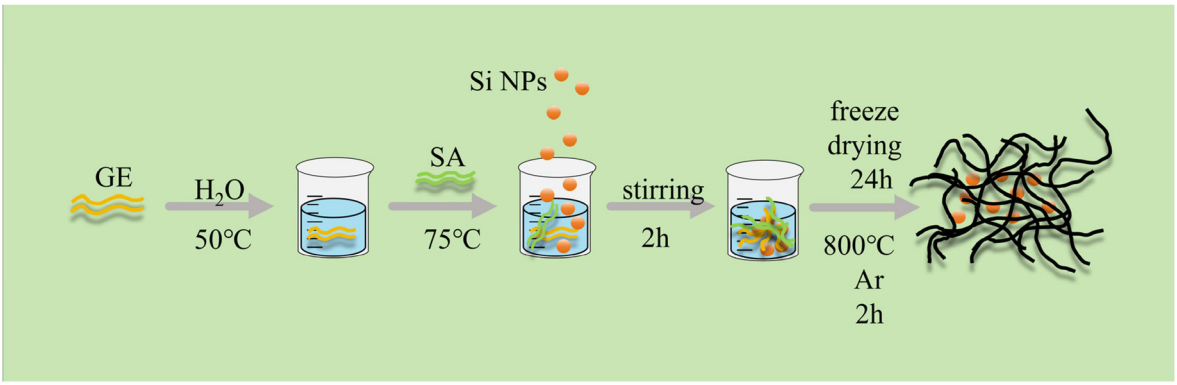

Fig. 1 Specific preparation process of the Si@C composite.

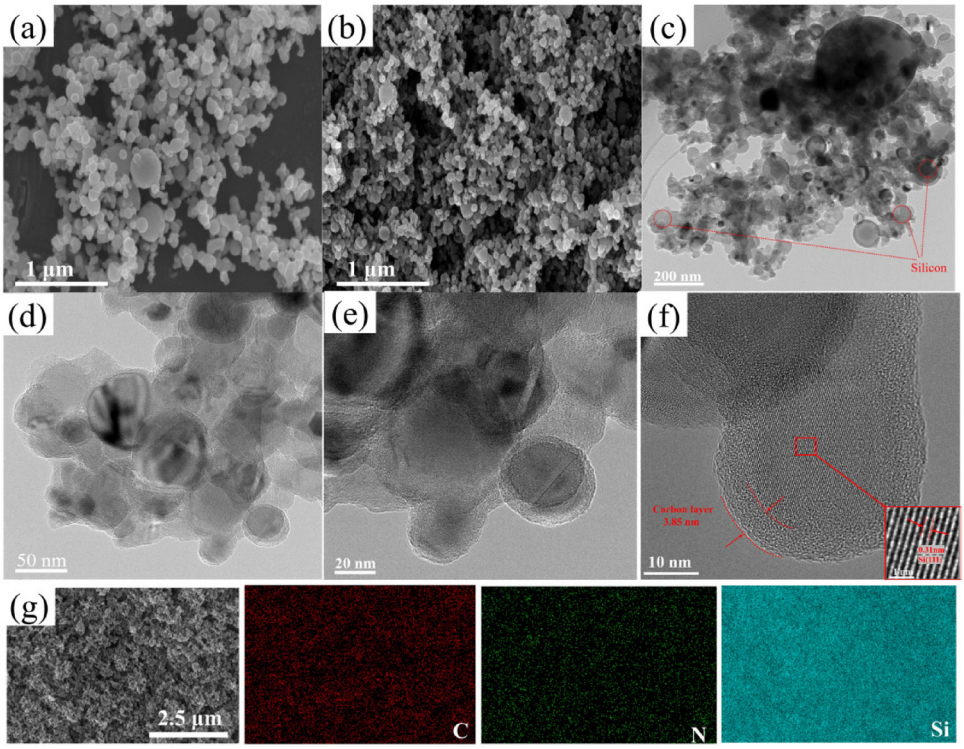

Fig. 2 SEM images of (a) Si NPs and (b) Si@C-GS; (c and d) TEM images of Si@C-GS. (e and f) HRTEM images of the corresponding regions; (g) SEM and EDS mappings of the corresponding regions of Si@C-GS.

which is a very important role. The corresponding EDS mappings are shown in Fig. 2(g); it is also further proved the homogeneous distribution of elements including C, N, and Si.

Fig. 3(a) shows the XRD patterns of Si, Si@C-G, Si@C-S, and Si@C-GS composites. All composite samples exhibit the same diffraction peaks as those of silicon appeared at 2θ = 28.6°, 47.2°, 56.1°, 69.1°, and 76.3°, which indicates that the crystalline phase of silicon has not been destroyed in spite of the multiple preparation steps.[36] In addition, all composites showed a broad peak at 2θ = 25° corresponding to that of graphite (002).[37] These results indicate that carbon formed a stable cladding structure with silicon particles. Fig. 3(b) shows the Raman spectra; the Si NPs and Si@C-GS show distinct characteristic peaks associated with silicon near 289 cm^{-1}, 509 cm^{-1}, and 936 cm^{-1}, and the peaks at 1333 cm^{-1} and 1583 cm^{-1} for the Si@C-GS mainly correspond to the peaks of carbon, which are referred to as the D peak and the G peak, respectively, indicating that the proportion of graphitization in the composite is not high.[38] In order to determine the chemical bonding states of Si@C-GS, we performed the determination by XPS, as shown in Fig. 3(c–e). The survey shows several peaks indicating the existence of Si, N, and O. Fig. 3(d) demonstrates the spectrum of Si 2p with four peaks at 99.2 eV, 99.7 eV, 102.3 eV, and 103.5 eV corresponding to Si–Si, Si–C, Si–O–C, and Si–O–Si.[39] Fig. 3(e) shows that the N 1s of Si@C-GS materials has peaks at 398.5 eV and 400.4 eV, corresponding to pyridnic N and pyrrolic N, respectively. Pyridnic N can enhance materials' electrochemical performance by increasing lithium ion storage sites.[40] The pore structure of Si@C-GS was analyzed using nitrogen adsorption–desorption curves, as shown in Fig. 3(f). It can be seen that the curve of Si@C-GS belongs is type IV. An obvious hysteresis loop is generated at high relative pressure, which is mainly related to the capillary coalescence of the mesopores. This result is consistent with the pore size distribution in the inset, indicating that the pore structure of Si@C-GS is mainly microporous and mesopores. The specific surface area of Si@C-GS composites was calculated as 26.51 m^2 g^{-1} by the Brunauer–Emmett–Teller (BET) method.[41] In order to fully investigate the electrochemical properties of Si@C-GS, they were assembled as half-cells to facilitate performance testing. In order to determine the Si content of the composites, we did a TGA test, as shown in Fig. 3(h). The weight loss of the composites in the figure is mainly the loss of carbon mass. Based on this, we can calculate the Si content contained in the composites, and the Si content of Si@C-GS, Si@C-G and Si@C-S is 84.8%, 84.3%, and 84.1%, respectively. The mass of Si increases with the temperature, which is mainly related to the oxidation in air.[42,43] In addition, we can see that there is a deviation in the Si content of the three groups of samples, which is mainly due to two reasons. On the one hand, it is because whether it is gelatin, sodium alginate, or a gelatin and sodium alginate composite, a kind of colloid is formed after the addition of deionized water, so there will be a certain fluctuation of their compo-

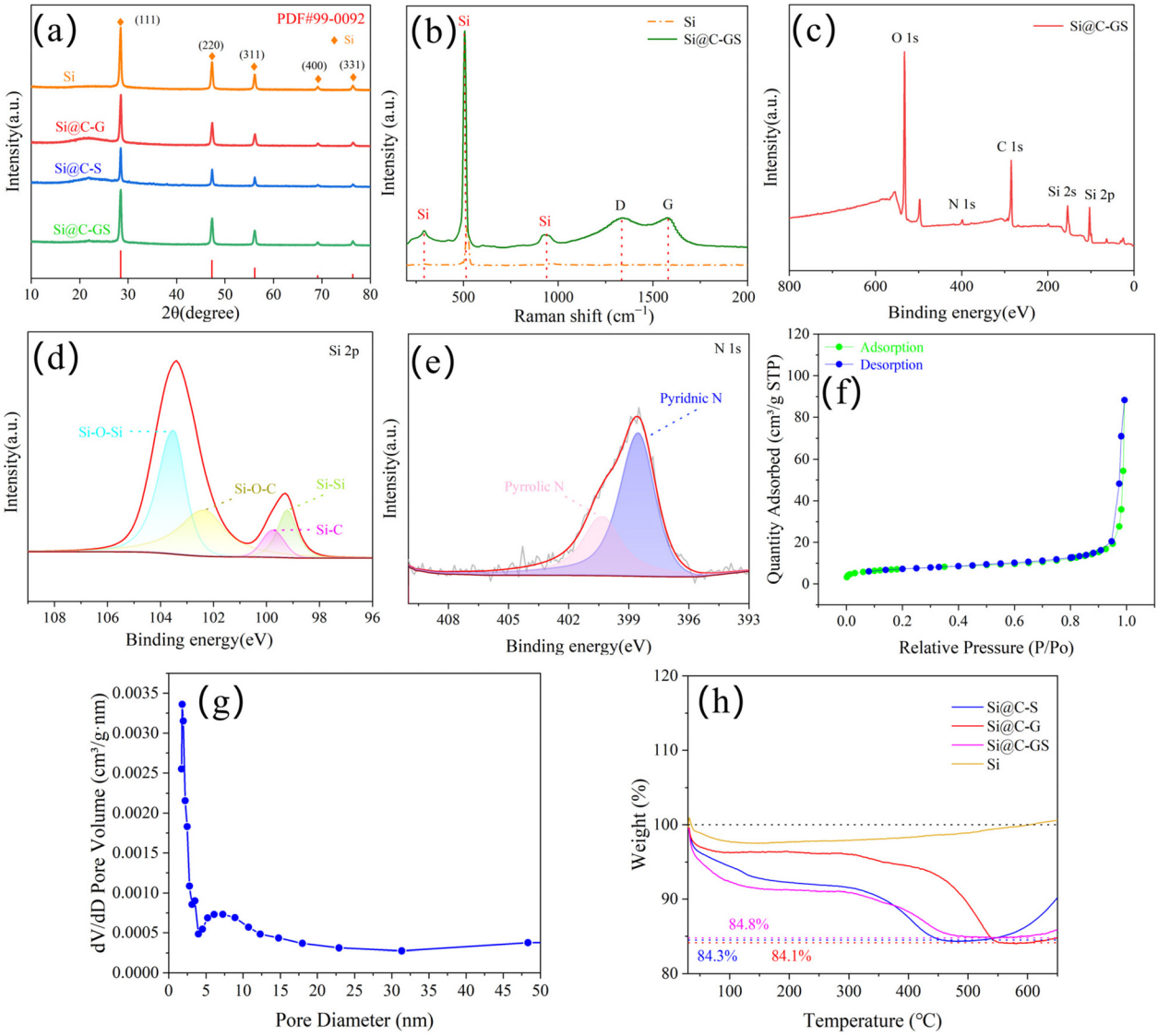

Fig. 3 (a) XRD patterns of Si NPs, Si@C-G, Si@C-S, and Si@C-GS. (b) Raman spectrum of Si NPs and Si@C-GS. (c) XPS survey spectrum and high-resolution spectrum (d) Si 2p, (e) N 1s of Si@C-GS. (f) Nitrogen adsorption/desorption isotherms of Si@C-GS. (g) Pore size distribution curve. (h) TGA curves under air.

sition content in the same volume as well as the same mass ratio. The other hand is that a certain degree of error exists in the testing of composites as well.

Fig. 4(a) shows the CV curves (the data we used were obtained from the second lap of the CV test) of Si@C-GS with a scan rate of 0.1 mV s^{-1} and a voltage range of 0.01 V–1.5 V. It can be seen that there are three distinct peaks during the first five cycles. A significant reduction peak occurs at 0.14 V; this is due to the alloying reaction of Si (Si → LiχSi). The oxidation peak corresponding to the delithiation process (LiχSi → Si) appears at 0.36 V and 0.52 V.[44] Meanwhile, both the oxidation and reduction peaks appear to increase with the increase of scanning cycles, which indicates that the capacity of the cell is further improved as the activation process proceeds. Fig. 4(b) shows the Nyquist plots of Si@C-S, Si@C-G, and Si@C-GS, which are mainly for further investigation of the surface dynamics of the electrodes. The high-frequency semicircle (R_{ct}) and the slanted straight line (Li^+ diffusion resistance) form the whole Nyquist curve.[45] The R_{ct} values of Si@C-S and Si@C-G are about 200 Ω, the R_{ct} value of Si@C-GS is about 250 Ω, and the R_{ct} value of Si NPs is about 450 Ω.[46] It can be seen that the impedance value decreases significantly after the introduction of the carbon coating. The carbon cladding improves the electrical conductivity of the composite, which in turn decreases the impedance. The Weber factor values (σ) of Si@C-GS, Si@C-G and Si@C-S were obtained by fitting the data in the low-frequency region, as shown in Fig. 4(c).

The Weber factor values of Si@C-GS, Si@C-G and Si@C-S are 410, 280, and 400, respectively, which are significantly smaller than that of Si NPs (σ = 640), which suggests that the

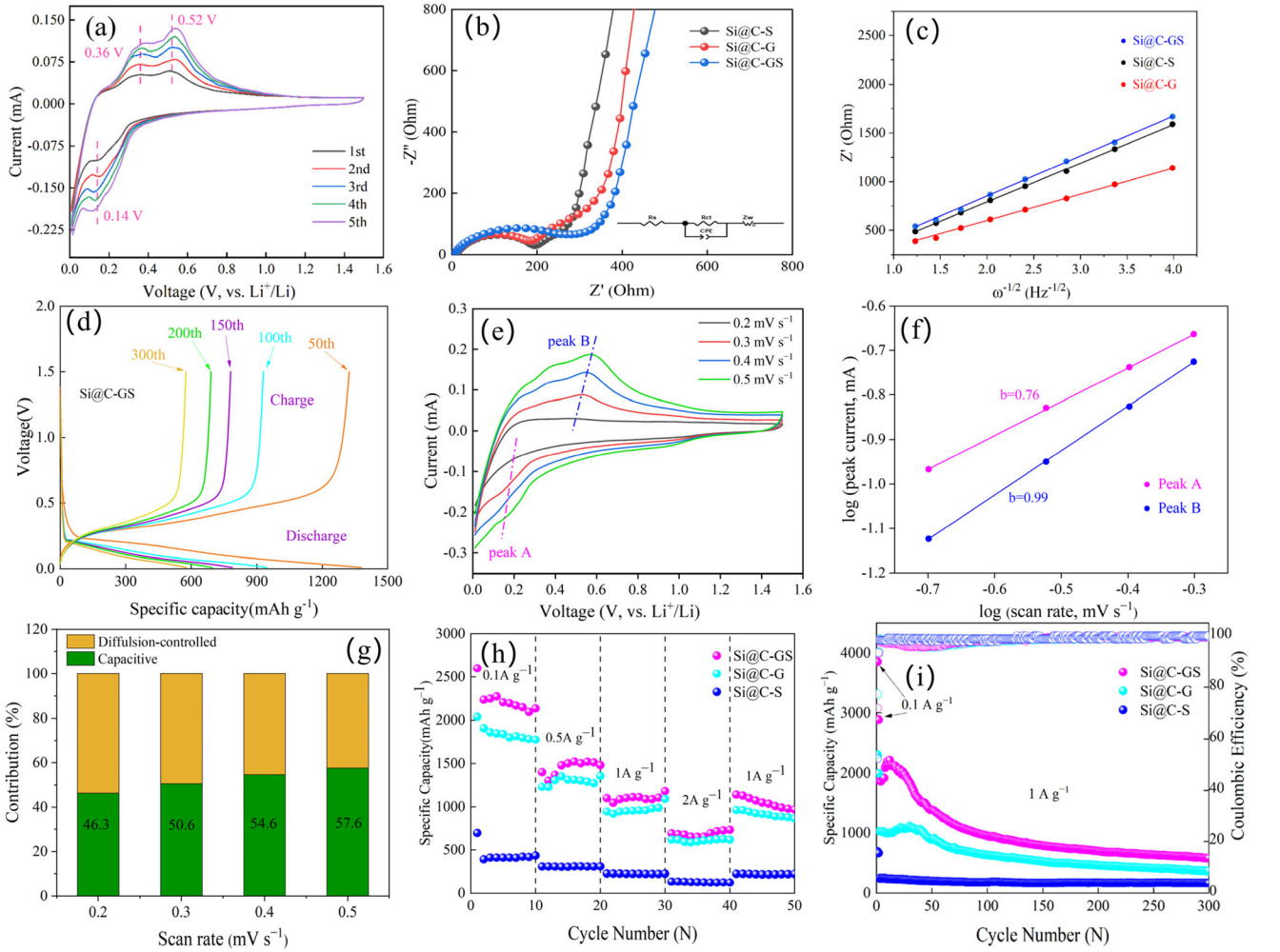

Fig. 4 (a) CV curves of Si@C-GS at 0.1 mV s^{-1}. (b) EIS of Si@C-S, Si@C-G, and Si@C-GS before cycling. (c) Fitted high frequency regions, before cycling. Linearly fitted Z' and $\omega^{-1/2}$ plots of Si@C-GS, Si@C-G and Si@C-S. (d) Charge/discharge curves of Si@C-GS at a current density of 1 A g^{-1}. (e) CV curves of Si@B-C/rGO from 0.2 to 0.5 mV s^{-1}. (f) Logarithm of peak current *vs.* logarithm of scan rate. (g) The proportion of pseudo capacitance and diffusion control in the total capacity. (h) Rate performance of Si@C-S, Si@C-G, and Si@C-GS at 0.1 A g^{-1}, 0.5 A g^{-1}, 1 A g^{-1}, and 2 A g^{-1} current densities. (i) Cycling performance of Si@C-S, Si@C-G, and Si@C-GS at a current density of 1 A g^{-1}.

introduction of composite carbon coatings improves the Li^+ diffusion ability of the material to a great extent and also explains the excellent electrochemical performance of Si@C-GS. The reason for the larger Weber factor of Si@C-GS than Si@C-G may be due to the fact that there are problems such as fluctuations in the quality of the composition due to the fact that the precursor of the material is a colloid formed by gelatin/sodium alginate added to deionized water. Also, it can be seen from the TGA curves that the silicon content of Si@C-GS is slightly higher than that of Si@C-G and Si@C-S, which explains the largest R_{ct} of Si@C-GS.

Pre-cycling charge/discharge curves of Si@C-GS show good performance at a current density of 0.1 A g^{-1} (see ESI, Fig. S2†). From the charge–discharge curves (Fig. 4d), the charge–discharge plateau is associated with silicon, indicating the successful doping of silicon. Also, the good cycling performance of Si@C-GS is further reflected by observing the charge–discharge curves. In order to investigate the electrochemical kinetics of Si@C-GS materials more deeply, CV tests were performed at different scan rates at 0.1–0.5 mV s^{-1}, as shown in Fig. 4(e). The results show that the storage behavior of Li^+ in the electrode materials is mainly characterized by the cell properties (diffusion-controlled) and pseudocapacitance properties (capacitance-controlled). The value of b can be calculated according to eqn (1).

$$i = av^b \tag{1}$$

The value of a in eqn (1) is a constant, so the value of b can be obtained by curve fitting, as shown in Fig. 4(f). The value of b is between 0.5 and 1; it can be seen that the lithium storage behavior of the electrode has both battery and pseudocapacitance characteristics. $I(V)$ refers to the total current, k_1v refers

to the pseudocapacitive contribution part, and $k_2v^{1/2}$ refers to the diffusion control contribution part (eqn (2)).

$$I(V) = k_1v + k_2v^{1/2} \quad (2)$$

As shown in Fig. 4(g), the percentage of pseudocapacitance contribution increases with the increase of the scan rate, which is as high as 57.6% at a scan rate of 0.5 mV s^{-1}. This result proves that the capacitance effect of the Si@C-GS electrode plays an important role at high scan rates.[47,48] Fig. 4(h) shows the rate performance tests of Si@C-G, Si@C-S, and Si@C-GS at current densities of 0.1 A g^{-1}, 0.5 A g^{-1}, 1 A g^{-1}, and 2 A g^{-1}. The rate performance of Si@C-GS is the most excellent. Its capacity decreases with the increase of the current density, but the average capacity is still as high as 686.6 mA h g^{-1} at a high current density of 2 A g^{-1}. When the current density recovered from 2 A g^{-1} to 1 A g^{-1}, the capacity also recovered rapidly, which indicated that Si@C-GS had excellent rate performance and still had a large reversible capacity under high current density. The good cycling and multiplicity performance of Si@C-GS was mainly related to the N-doped carbon coating. The three-dimensional carbon network coating structure had a good pore structure, thus facilitating ion diffusion as well as improving the electrical conductivity of the material. At the same time, it effectively inhibits the continuous fragmentation of silicon particles. The cycling performance of Si@C-G, Si@C-S, and Si@C-GS is plotted in Fig. 4(i). It can be seen that Si@C-GS exhibits excellent cycling performance, with a reversible capacity of 1865 mA h g^{-1} in the first cycle at a current density of 1 A g^{-1} and a coulombic efficiency of 98%. The capacity is maintained at 580 mA h g^{-1} after a long period of up to 300 cycles. These results indicate that Si@C-GS has good cycling reversibility. Si@C-G also showed good cycling performance, but the reversible capacity was lower, which was only 365 mA h g^{-1} after 300 cycles. We speculated that Si NPs were not uniformly coated by the carbon for Si@C-G, and the volume expansion phenomenon was not suppressed, which led to rapid capacity degradation and low reversible capacity. The reversible capacity of Si@C-S composites is only 692 mA h g^{-1} in the first cycle, and then remains at a low level. It should be explained that its carbon coating is too thick and non-uniform, which hinders the ion diffusion, and thus affects the normal release of the silicon capacity.

4. Conclusions

In summary, we have successfully prepared N-doped Si@C composites as high-performance anodes for lithium-ion batteries. The particular Si@C-GS composite anode exhibits the largest specific capacity of 2230 mA h g^{-1} at 0.1 A g^{-1} and still maintains 686.6 mA h g^{-1} at 2 A g^{-1}. Moreover, the reversible capacity of the anode was maintained at 580 mA h g^{-1} after 300 cycles at a current density of 1 A g^{-1}. The satisfactory specific capacity, excellent rate performance, and cycling stability of this half-cell are attributed to the combined action of the GE + SA precursor and Si NPs, as well as the N-doped carbon 3D network coating formed by subsequent processing. It improves the ionic conductivity and electrical conductivity of the composites and accommodates the volume expansion of silicon, thus enhancing the cycling and rate properties of the anode. This novel Si@C material preparation process also provides a feasible way for the industrialization of silicon-based composites.

Author contributions

Liyang Lin: conceptualization, funding acquisition, and writing – review & editing; Mengjun Li: investigation, methodology, writing – original draft, validation and formal analysis; Ying Yan: formal analysis; Yuanhao Tian: methodology; Juan Qing: formal analysis; Susu Chen: conceptualization, data curation and writing – review & editing.

Data availability

The data supporting this article have been included as part of the ESI.†

Conflicts of interest

The authors declare no conflict of interest associated with this article.

Acknowledgements

This work was supported by the Science and Technology Research Program of Chongqing Municipal Education Commission (grant no. KJZD-K202200702), the Natural Science Foundation of Chongqing (grant no. CSTB2024NSCQ-MSX0429, CSTB2022NSCQ-LZX0068), the Natural Science Ranking Projects of Chongqing Jiaotong University (grant no. XJ2023000701), and the Eagle Plan Research Project of Chongqing Municipal Education Commission (CY240704). We would like to acknowledge the contributions of Qinyuan Tian, Jiayi Liu, Xiaoyuan Zhou, and Wenquan Cai.

References

1 J. W. Fergus, *J. Power Sources*, 2010, **195**, 939–954.
2 K. Jian, Z. H. Chen and X. B. Meng, *ChemElectroChem*, 2019, **6**, 2825–2840.
3 Q. Sun, K. C. Lau, D. Geng and X. Meng, *Batteries Supercaps*, 2018, **1**, 40–40.
4 Z. Liang, F. Du, N. Zhao and X. Guo, *Chin. J. Struct. Chem.*, 2023, **42**(11), 100108.

5 H. Lü, X. Chen, Q. Sun, N. Zhao and X. Guo, *Acta Phys.-Chim. Sin.*, 2024, **40**(3), 2305016.
6 K. Guo, B. Xi, R. Wei, H. Li, J. Feng and S. Xiong, *Adv. Energy Mater.*, 2020, **10**(12), 1902913.
7 S. Goriparti, E. Miele, F. De Angelis, E. Di Fabrizio, R. Proietti Zaccaria and C. Capiglia, *J. Power Sources*, 2014, **257**, 421–443.
8 C. Wang and Y. Chen, *Appl. Energy*, 2024, **365**, 123280.
9 H. Liao, W. Zhong, C. Li, J. Han, X. Sun, X. Xia and Y. Zhang, *J. Energy Chem.*, 2024, **89**, 565–578.
10 N. Obrovac and L. Christensen, *Electrochem. Solid-State Lett.*, 2004, **7**, A93.
11 M. Park, J. H. Kim, H. Kim and H. J. Sohn, *Chem. Soc. Rev.*, 2010, **39**, 3115–3141.
12 H. Cai, K. Han, H. Jiang, J. Wang and H. Liu, *J. Phys. Chem. Solids*, 2017, **109**, 9–17.
13 W. Cao, M. Chen, Y. Liu, K. Han, X. Chen, H. Ye and S. Sang, *Electrochim. Acta*, 2019, **320**, 134615.
14 H. Jiang, X. Zhou, G. Liu, Y. Zhou, H. Ye, Y. Liu and K. Han, *Electrochim. Acta*, 2016, **188**, 777–784.
15 W. Y. Cao, K. Han, M. Chen, H. Ye and S. Sang, *Electrochim. Acta*, 2019, **320**, 134613.
16 R. Fang, C. Miao, H. Mou and W. Xiao, *J. Alloys Compd.*, 2020, **818**, 152884.
17 N. Xia, Y. Li, Z. Zhou, Y. Wu, N. Zhou, H. Zhang and X. Xiong, *Ceram. Int.*, 2019, **45**, 1950–1959.
18 K. Chan, H. Peng, G. Liu, K. McIlwrath, X. F. Zhang, R. A. Huggins and Y. Cui, *Nat. Nanotechnol.*, 2007, **3**, 31.
19 H. Kim, M. Seo, M. H. Park and J. Cho, *Angew. Chem., Int. Ed.*, 2010, **49**, 2146–2149.
20 I. K. Yoo, J. Kim, Y. S. Jung and K. Kang, *Adv. Mater.*, 2012, **24**, 5452–5456.
21 X. Zhou, K. Han, H. Jiang, Z. Liu, Z. Zhang, H. Ye and Y. Liu, *Electrochim. Acta*, 2017, **245**, 14–24.
22 D. Ouyang, B. Liu, J. Huang and Z. Wang, *Process Saf. Environ. Prot.*, 2024, **185**, 76–85.
23 W. Wang and P. N. Kumta, *ACS Nano*, 2010, **4**, 2233–2241.
24 H. Zhang, X. F. Zhang, H. Jin, P. Zong, Y. Bai, K. Lian, H. Xuand and F. Ma, *Chem. Eng. J.*, 2019, **360**, 974–981.
25 F. Sun, K. Huang, X. Qi, T. Gao, Y. P. Liu, X. H. Zou, X. L. Wei and J. X. Zhong, *Nanoscale*, 2013, **5**(18), 8586–8592.
26 P. H. Camargos, P. H. J. dos Santos, I. R. dos Santos, G. S. Ribeiro and R. E. Caetano, *Int. J. Energy Res.*, 2022, **46**, 19258–19268.
27 M. G. Jeong, H. L. Du, M. Islam, J. K. Lee, Y. K. Sun and H. G. Jung, *Nano Lett.*, 2017, **17**(9), 5600–5606.
28 H. Dong, X. L. Fu, J. Wang, P. Wang, H. Ding, R. Song, S. M. Wang, R. R. Li and S. Y. Li, *Carbon*, 2021, **173**, 687–695.
29 X. Xu, Y. Dong, Q. Hu, N. Si and C. Zhang, *Energy Fuels*, 2024, **38**(9), 7579–7613.
30 H. Zhao, G. Zhao, F. Liu, T. Xiang, J. Zhou and L. Li, *J. Colloid Interface Sci.*, 2024, **666**, 131–140.
31 W. Y. Long, B. Z. Fang, A. Ignaszak, Z. Z. Wu, Y. J. Wang and D. Wilkinson, *Chem. Soc. Rev.*, 2017, **46**(23), 7176–7190.
32 D. Sui, M. Yao, L. Q. Si, K. Yan, J. G. Shi, J. S. Wang and Y. S. Zhang, *Carbon*, 2023, **205**, 510–518.
33 L. B. Li, S. Luo, Z. K. Zheng, K. N. Zhong, W. L. Huang and Z. Fang, *Ionics*, 2022, **28**, 161–172.
34 Y. C. Zhang, Y. You, S. Xin, Y. X. Yin, J. Zhang, P. Wang, X. S. Zheng, F. F. Cao and Y. G. Guo, *Nano Energy*, 2016, **25**, 120–127.
35 Y. L. Zhang, Z. J. Mu, J. P. Lai, Y. G. Chao, Y. Yang, P. Zhou, Y. J. Li, W. X. Yang, Z. H. Xia and S. J. Guo, *ACS Nano*, 2019, **13**(2), 2167–2175.
36 T. Mu, P. Zuo and S. Lou, *Chem. Eng. J.*, 2018, **341**, 37–46.
37 Q. Li, J. H. Mu, J. Zhou, Y. Zhao and S. P. Zhuo, *J. Electroanal. Chem.*, 2019, **832**, 284–292.
38 W. Zhang, J. J. Li, P. Guan, C. X. Lv, C. Yang, N. Han, X. C. Wang, G. J. Song and Z. Peng, *J. Alloys Compd.*, 2020, **835**, 155135.
39 W. J. Zhou, J. Z. Chen, X. W. Xu, X. Han, M. F. Chen, L. Yang and S. I. Hirano, *ACS Appl. Mater. Interfaces*, 2021, **13**, 15216–15225.
40 X. C. Qiu, X. F. Zhang and S. H. Yang, *Phys. Chem. Chem. Phys.*, 2011, **13**(27), 12554–12558.
41 K. Wang, S. E. Pei, Z. S. He, L. A. Huang, S. S. Zhu, J. F. Guo, H. B. Shao and J. M. Wang, *Chem. Eng. J.*, 2019, **356**, 272–281.
42 X. Xue, X. Liu, B. Lou, Y. X. Yang, N. Shi, F. S. Wen, X. J. Yang and D. Liu, *J. Energy Chem.*, 2023, **84**, 292–302.
43 W. Zhang, S. W. Gui, Z. H. Zhang, W. M. Li, X. X. Wang, J. H. Wei, S. B. Tu, L. X. Zhong, W. Yang and H. Yang, *Small*, 2023, **19**, 2303864.
44 L. Pan, H. B. Wang, D. C. Gao, S. Y. Chen, L. Tan and L. Li, *Chem. Commun.*, 2014, **50**(44), 5878–5880.
45 R. Ruffo, S. S. Hong, C. K. Chan, R. A. Huggins and Y. Cui, *J. Phys. Chem. C*, 2009, **113**(26), 11390–11398.
46 X. X. Xu, F. Z. Wu, W. L. Yang, X. Y. Dai, T. H. Wang, J. W. Zhou, J. Wang and D. Guo, *ACS Sustainable Chem. Eng.*, 2021, **9**(39), 13215–13224.
47 J. Pan, C. Sun, X. Zhao, J. Liu, C. Wang, C. Jiao, J. Sun and Q. Wang, *Mater. Today Sustainability*, 2023, **24**, 100503.
48 C. X. Sun, J. H. Pan, X. S. Zhao, C. X. Jiao, W. K. Yao, C. K. Wang, X. M. Fu, D. C. Ma, H. C. Xue, J. J. Liu, L. Y. Cui, M. Li, A. Du and Q. Wang, *J. Alloys Compd.*, 2023, **968**, 171922.